Heliyon 9 (2023) e13176

Contents lists available at ScienceDirect

Heliyon

journal homepage: www.cell.com/heliyon

Research article

Fabrication of polycaprolactone/calcium phosphates hybrid scaffolds impregnated with plant extracts using 3D printing for potential bone regeneration

Claudia Garcia [a,*], Yeison Orozco [b], Alejandra Betancur [b], Ana Isabel Moreno [b], Katherine Fuentes [c], Alex Lopera [d], Oscar Suarez [e], Tatiana Lobo [f], Alexander Ossa [g], Alejandro Peláez-Vargas [h], Carlos Paucar [i]

[a] *Universidad Nacional de Colombia sede Medellín, Physics school, Grupo de Materiales Cerámicos y Vítreos, Colombia*
[b] *Universidad Nacional de Colombia sede Medellín, Grupo de Materiales Cerámicos y Vítreos, Colombia*
[c] *Universidad Nacional de Colombia sede Medellín, Colombia*
[d] *Grupo de Nanoestructuras y Física Aplicada (NANOUPAR), Dirección Académica, Universidad Nacional de Colombia, Sede de La Paz, Km 9 vía Valledupar La Paz, La Paz 202010, Colombia*
[e] *Universidad Nacional de Colombia sede Orinoquia, Colombia*
[f] *Universidad Nacional de Colombia sede Medellín, Chemistry school, Colombia*
[g] *School of Applied Sciences and Engineering, Universidad Eafit, Medellín, Colombia*
[h] *Universidad Cooperativa de Colombia, Medellín, Colombia*
[i] *Universidad Nacional de Colombia sede Medellín, Chemistry school, Grupo de Materiales Cerámicos y Vítreos, Colombia*

ARTICLE INFO

Keywords:
Scaffold
3-D printing
Natural extracts
Impregnation method
Polycaprolactone
Calcium phosphate

ABSTRACT

The increase in critical bone diseases and defects in the world's population increases the need for bone substitutes to restore form and function. Organic and inorganic scaffolds with antibacterial properties could provide advantages for bone regeneration. In this study, we obtained scaffolds of polycaprolactone (PCL) charged with calcium phosphates nanoparticles and impregnated with extracts of Colombian plants as an alternative for potential bone regeneration. Calcium phosphate nanoparticles were obtained via auto-combustion synthesis. The nanoparticles were incorporated into the PCL with a chemical dissolution-disperse process. The composite obtained was used to produce a filament to print Triply Periodic Minimal Surface (TPMS) based scaffolds. Such geometry facilitates cellular growth thanks to its interconnected porosity. The scaffolds were impregnated with extracts of *Justicia* cf *colorifera* (Acanthaceae), and *Billia rosea* (Sapindaceae) due to their ancestral medical applications. A physical and biological characterization was conducted. The process to print scaffolds with an enhanced geometry to facilitate the flux of biological fluids was successful. The scaffolds loaded with *B. rosea* showed strong antibacterial behavior, suggesting the presence of reported terpenoids with antibacterial properties. The approach used in this study evidenced promising prospects for bone defect repair.

* Corresponding author. Universidad Nacional de Colombia sede Medellín, Carrera 65 # 59A-100, Medellín, Colombia.
E-mail addresses: cpgarcia@unal.edu.co (C. Garcia), yaorozcoo@unal.edu.co (Y. Orozco), albetancurpa@unal.edu.co (A. Betancur), animorenofl@unal.edu.co (A.I. Moreno), kfuentesar@unal.edu.co (K. Fuentes), aalopera@unal.edu.co (A. Lopera), oesuarezmo@unal.edu.co (O. Suarez), tloboech@unal.edu.co (T. Lobo), eossa@eafit.edu.co (A. Ossa), alejandro.pelaezv@campusucc.edu.co (A. Peláez-Vargas), cgpaucar@unal.edu.co (C. Paucar).

https://doi.org/10.1016/j.heliyon.2023.e13176
Received 8 October 2022; Received in revised form 19 January 2023; Accepted 20 January 2023
Available online 25 January 2023

1. Introduction

Bone is formed by an elegant hierarchical arrangement of simple organic and inorganic materials providing its outstanding mechanical properties [1,2] The use of temporary scaffolds has become a common practice to help on bone regeneration.

Important features of the scaffolds as porosity and its interconnectivity have proved to be crucial to cell adhesion and proliferation, as well as to the diffusion of nutrients and oxygen through the structure [3]. Indeed, the ability for cell fixation, proliferation, differentiation and further invasion -leading to vascularization-to an scaffold is governed by its microstructure and porosity [4]. It is then required to design and manufacture bone reconstruction biomaterials with proper three-dimensional (3D) structures with the pore volume and size required to accomplish its desired function. Furthermore, the scaffold topography must allow cell migration and growth of new tissues while the diffusion of nutrients, soluble factors and bio-products should be able to diffuse effortlessly through the pores [4].

The absence of spatial growth of the cells force the porous structure of the scaffolds to be responsible for defining the anatomical shape of the tissue, guiding the cells during healing [5]. Scaffolds' permeability and its pore interconnectivity have to ensure cellular growth, tissue proliferation and transport of nutrients [6]. Further, geometric attributes as concave surface curvatures and pore shape and sizes with values between 300 and 1200 μm are considered as essential in ensuring a good performance of the scaffold [7]. It has been found by several authors that Triply Periodic Minimal Surfaces (TPMS) are able to provide high surface-to-volume ratios, good pore connectivity, and variable conductivity, making them an appropriate option for bone regeneration [8]. Additive manufacturing uses CAD/CAM procedure to fabricate three-dimensional bodies with complex geometries. These characteristics of additive manufacturing have received significant attention in the biomedical industries [9]. 3D printing facilitates the control of geometric parameters, making possible the fabrication of complex geometries like TPMS [10].

A good scaffold design, mimicking the native bone tissue, requires suitable materials offering cell adhesion and proliferation while providing the required structural strength to support the external loads [11–14] One of the most commonly used biomaterials in bone regeneration due to its cost-efficiency, toughness, flexibility, biodegradability and bioresorbability is the semicrystalline Poly (ε-caprolactone) (PCL) [2,4,15]. Furthermore, it has been found that blends of PCL with inorganic components (e.g: Calcium phosphates) can improve considerably the mechanical and biological responses of scaffolds. It is then expected that PCL filaments loaded with inorganic and biocompatible particles can provide a good alternative for the fabrication of scaffolds with enhanced mechanical and biological. Calcium phosphates are the main inorganic components of the extracellular matrix of hard tissues like bone and teeth and further support the cellular development of the mature extracellular matrix. Due to their excellent biocompatibility, these ceramic materials have been extensively used in biomedical and biological applications world [16,17]. The synthesis route used to produce calcium phosphates has a direct effect on their chemical composition and physical properties [18]. Synthesis of calcium phosphates via solution-combustion has shown to allow the production of nanometric particles favorable to be used in the fabrication of filaments.

Colonization or infectious diseases are the most frequent complication in surgeries associated with antimicrobial resistance in hospitals [19]. Additionally, it is increasingly common to find bacteria resistant to traditional antibiotics giving rise to dangerous public health problem [12]. An essential and important attribute of scaffolds should be their bacteriostatic, and even bactericidal, properties. Accordingly, to overcome limitations concerning antimicrobial bioactivity, a scaffold could be modified by enriching it with therapeutic agents with bacteriostatic or bactericidal properties. Currently, several antibiotics, such as metronidazole, amoxicillin, ampicillin, and tetracycline, are commonly used to produce modified scaffolds [20,21]. More recently, natural substances have been studied, from lichen extracts [22], garlic (*Allium sativum*) and ginger essential oils (*Zingiber officinale*) [23], crude extracts from *Spinacia oleracea,* and *Cissus quadrangularis* [24,25], have been reported to improve biological response scaffolds. Considering the low phytotoxicity of natural products, as well as their inherent sustainability, they could be a successful source of antibacterial agents. Being Colombia the second largest biodiverse country in the world, the exploration of antimicrobial plant-derived products constitutes an alternative of developing hybrid scaffolds with less infectious rates.

In this paper, we studied the obtention of scaffolds in the form of a TPMS Gyroid made of PCL with calcium phosphates (CP) nanoparticles using 3D printing, and modified with plant-derived extracts of *Justicia* cf *colorifera* V.A.W. Graham (Acanthaceae), and *Billia rosea* (Planch. & Linden) C. Ulloa & Jorg. (Sapindaceae) to improve its antibacterial behavior.

2. Materials and methods

2.1. Materials

Pellets of poly-e-caprolactone (PCL, MW 80,000. *Sigma-Aldrich*) were used as raw material in the fabrication of filaments. A mixture of ethanol (C_2H_5OH, *Merck*), dichloromethane (CH_2Cl_2, *Loba Chemie*), and tetrahydrofuran (C_4H_8O, *Merck*) was used to dissolve the PCL. Calcium nitrate tetrahydrate ($Ca(NO_3)_2.4(H_2O)$, *Merck*), diammonium hydrogen phosphate ($(NH_4)_2HPO_4$, *Scharlau*), nitric acid (HNO_3, *Merck*), and glycine (C_2H5NO2 Gly, *Aesar Alfa*) were used to obtain calcium phosphates nanoparticles [16,26].

2.2. Synthesis of calcium phosphates nanoparticles

Calcium phosphates were obtained via auto-combustion synthesis as described [18]. Briefly, diammonium hydrogen phosphate and calcium nitrate were mixed in distilled water under constant stirring, maintaining a ratio of Ca/P = 1.6 until the formation of a precipitate subsequently dissolved with nitric acid (HNO_3). The glycine (fuel) was added in oxidizer-to-fuel ratio O/F = 1. The final

solution was maintained at approximately 80 °C on a hot plate under stirring until a gel appeared. Then the temperature of the gel was increased to 200°C–250 °C until gel ignition and ash formation. The ash was subjected to thermal treatment at 800 °C for 2 h. A white powder was recovered and submitted to structural and morphology characterization. Internal structure of particles was characterized by means of X-Ray diffraction in a D8 Advance Eco Bruker model diffractometer from Bruker (Karlsruhe, Germany Cu Ka, 1.5418 Å, between 10 and 50° (2θ)).

2.3. Preparation of the PCL/Calcium phosphates (CP) composite material

20% w/w of calcium phosphates particles were incorporated into the PCL with a chemical dissolution-disperse process. Calcium phosphate nanoparticles were treated in a Planetary Ball Mill (Retsch PM 100) for 20 min in cycles of 5 min with turn inversion at 200 rpm. The nanoparticles were mixed with ethanol using an ultrasonic processor Cole Parmer model CV334 at 500 W and 20 kHz for 5 min, with cycles of 20 s and 5 s of pause. Then, a mixture of dichloromethane and tetrahydrofuran was added and the resulting suspension was heated at 40 °C and periodically stirred every 15 min for 5 h. The resulting liquid was spread on a flat surface generating sheets of approximately 1 mm thickness, which were dried at room temperature for one day. The PCL/Calcium phosphates sheets were cut into small pieces and used to fabricate the filament.

2.4. Filament production

The commercial PCL and the PCL/CP composites were processed using a Wellzoom C extruder at 90–100 °C. At these temperatures the PCL reaches its melting point, and the remaining solvents evaporate. A speed of push and pull of 2000 mm/min was used to obtain two types of filaments: one without particles of calcium phosphates and another one with 20% w/w of particles of calcium phosphates with a diameter of 1.75 mm ± 0.2 mm.

2.5. 3D printing scaffolds from PCL/calcium phosphates

Scaffolds based on TPMS gyroid were designed using MathMod, Blender, and Prusaslicer [8] for the different assays made in this paper. An advantage of 3D printing over conventional processing techniques is the ability to control the porosity and porosity density within the scaffold [27]. In the process of designing the scaffold, a code is established and read by the printer that defines the orientation of the adjacent lines to be printed as well as the distance between them, which determines the porosity and density of the final product. In our case, a scaffold with a 3 mm side base unit composed of two printing lines of 0.75 mm thickness each was designed. That unit is repeated as many times as necessary to result in a mesh of lines and holes of 15 mm outer side, composed of 10 lines of 0.75 mm thickness each. The figure was designed for a porosity of 50%. Scaffolds were printed in an Anycubic Chiron 3D printer modified for direct extrusion using a 1.75 nozzle with an extruder temperature of 80 °C, bed temperature of 40 °C, general print speed of 20 mm/s, and modified material flux of 120%. For the swelling and degradation experiments, parallelepiped scaffolds of 7.5 mm × 7.5 mm x 2 mm were obtained. Contact angle tests were done using solid disks with diameters of 15 mm and 2 mm in height. Cubes of 15 mm × 15 mm x 15 mm were printed for mechanical tests. Solid cylinders with a diameter of 8 mm and 3 mm in height were used for the biological tests and for the SEM tests were used parallelepiped scaffolds of 15 mm × 15 mm x 2 mm.

2.6. Plant material

2.6.1. Plant species

Justicia cf *colorifera* (V.A.W. Graham) (Acanthaceae), and *Billia rosea* (Planch. & Linden) C. Ulloa & Jorg. (Sapindaceae) were selected for this study based on different criteria. The species *J.* cf. *colorata* is used traditionally for microbial infections in the Orinoquia region of Colombia, where it is called “antibiotic”. It was collected at the medicinal plant garden of the National University of Colombia - Arauca branch at 125 m.a.s.l. (7°00′59″N 70°44′40″W). *B. rosea* was selected from a pool of extracts for its preliminary antimicrobial activity. This plant was collected in the Andean region at 2928 m.a.s.l. (6º61′ N, 75º65’ W, Belmira, Colombia). Voucher samples of both species were collected for the accurate identification of the plants. *B. rosea* was deposited at the botanical garden herbarium (JAUM-Joaquin Antonio Uribe de Medellin, Colombia) with accession number LB-2043, and *J.* cf. *colorata* was compared with the voucher deposited in the herbarium (Universidad Nacional de Colombia, Orinoquia Branch).

For both species, a mix of leaves and twigs (1.5 kg of each) were collected, air-dried, and milled. Each of the species was extracted three times with 90% ethanol (1 L x 100 g) at room temperature for 24 h. The combined ethanol extract of each species was filtered and concentrated at a temperature below 50 °C to a semisolid paste using a rotary evaporator (Heidolph HEI-VAP).

2.7. Impregnation of scaffolds with J. cf colorifera and B. rosea ethanol-soluble extracts

The dried semisolid paste of each plant extract was re-dissolved in absolute ethanol for the impregnation of the scaffolds. For *J.* cf. *colorata* a solution of 40% w/v was prepared, while for *B. rosea* the final concentration of the solution was 20% w/v. For the impregnation of the extracts in the discs, a drop of 20 μL was added, and placed in a positive pressure chamber (Wiropress, BEGO) for 3 min. After verification that the extract was absorbed by the material, the process is repeated, until the incorporation of 40 μL. The same process was carried out for both extracts.

Fig. 1 outlines the process for obtaining PCL scaffolds with calcium phosphate particles impregnated with plant extracts.

2.8. Antibacterial screening

Streptococcus mutans (ATCC25175) and *Staphylococcus aureus* (ATCC25175) were selected as the most widely described biofilm models, to assess the antibacterial properties of the extracts, surface of control, and experimental scaffolds. Bacteria were grown in brain-heart infusion (BHI) agar at 37 °C. After 24 h, bacterias were re-suspended in physiologic saline solution (0.9% NaCl in PBS) to obtain a concentration of 1 × 109 UFC/ml according with CLSI [21].

To conduct a rapid screening of the antimicrobial activity of the extracts, the Kirby-Bauer diffusion susceptibility test was performed [22]. The test was carried out using Mueller Hinton Agar (Scharlau, Barcelona). As positive and negative control chlorhexidine digluconate (Farpag, Col) and DMSO were used, respectively.

The determination of the minimum inhibitory concentration (MIC) was calculated by microdilution method [23]. Briefly, different extract preparations were subjected to a serial dilution using sterile nutrient broth medium to obtain final concentrations of the extracts between 50% w/v to 1% w/v. The bacterial suspension (20 μL/mL broth) was inoculated in 96-well plates, homogenized, and incubated at 37 °C for 24 h. The bacterial growth was indicated by turbidity. and incubated at 37 °C for 24 h. The bacterial growth was indicated by turbidity. The MIC value was recorded as the lowest dilution of each extract where no growing was observed. Each test was performed in triplicate and repeated twice. A control experiment was run in parallel to study the impact of the solvent itself (without extract) on the growth of the test bacteria.

Furthermore, discs and scaffolds with different experimental conditions were sterilized using ethanol 70%. All experiments were performed following a previously reported sequence [24]. After allowing bacterial growth overnight, areas of clear media surrounding the disks were measured to calculate the inhibition area compared to the positive control. The zones of inhibition were measured using the ImageJ software. All bioassays performed in triplicate.

2.9. Plant extract characterization

Extracts were analyzed using a gas chromatograph (Agilent 6890), coupled with a mass spectrometer (Agilent 5973) (GC-MS). For this procedure a capillary column of fused silica DB-1MS (Agilent 123–5536, 0.25 mm × 30 m x 0.25 μm) covered with 5% phenyl methyl siloxane, was used. Extracts of *J.* cf *colorifera* and *B. rosea* were diluted in methanol and 1.0 μL of each, was injected using helium gas grade 5 (AGA Fano S.A., UAP 99.999%) at a flux of 1.2 mL min-1 (linear velocity 37 cm/s). The splitless mode was used, electron ionization (EI), with an initial temperature of 50 °C, raised by 2 °C per minute to a maximum of 300 °C for 62 min. The run was performed using the SCAN mode between *m/z* 30–800.

The chromatograms were analyzed with OpenChrom software and the compound's identity was assigned by comparison of its mass spectral fragmentation patterns with those stored in the National Institute Standard and Technology spectral library (NIST) [25].

2.10. Scaffolds characterization

2.10.1. Scanning electron microscopy (SEM)

A JEOL JSM-7100 F microscope was used to observe morphology of the filaments and scaffolds. The microscope was equipped with an energy dispersive X-ray spectroscopy (EDX) Oxford X-Max model 51-XMX1178. All samples were coated with carbon.

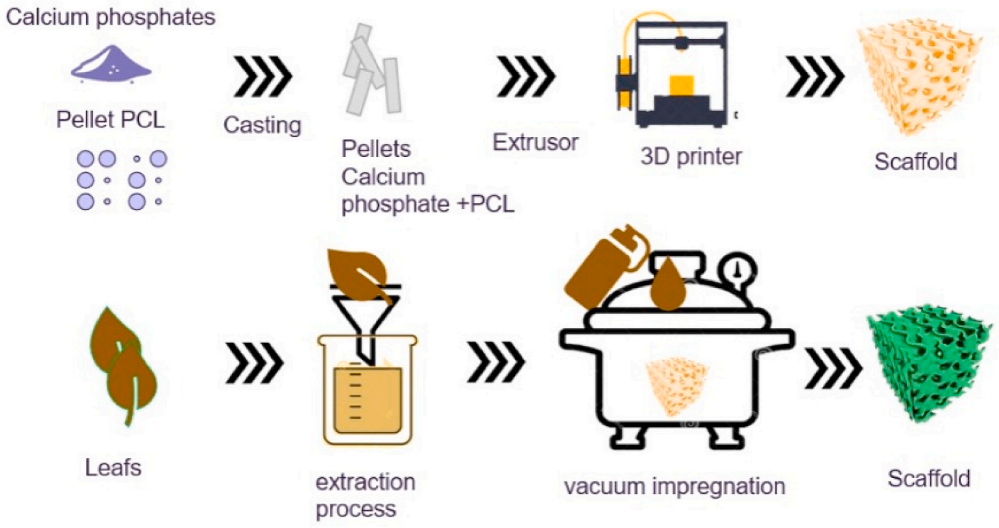

Fig. 1. Fabrication of 3D printed PCL/Calcium Phosphates scaffolds and their extracts impregnation process.

2.10.2. Swelling experiment

The swelling ratio (SR) was measured by immersing the dry samples in PBS at 37 °C for 4, 8, 12, 24, 28, 32, 36, 48, 52, 56, 60 and 72 h. A paper napkin was used to get excess PBS from the samples. The swollen samples were weighed, and the swelling ratio was then calculated according to equation (1) [10,28].

$$Swelling\ ratio\ (\%) = \left(\frac{W_s - W_D}{W_D}\right) x100 \quad \text{Eq. 1}$$

Where W_s is the weight in the swollen samples at a given time and W_D is the dry weight of samples.

2.10.3. Contact angle test

The hydrophilicity of the samples was measured using the contact angle formed between a water drop at room temperature and surface of selected scaffolds. To do this, a Canon EOS R7 digital camera was used to obtain images, and the Image J software was used to measure the formed angle. The test was performed five times for both materials, and the average angle was reported. Two-sample *t*-test was performed to probe the difference between samples.

2.10.4. Degradation rate test

Scaffolds degradation ratio was calculated by immersing each scaffold in a 2 mL PBS solution followed by incubation at 37 °C. Scaffolds were dried at specific time points including 7, 14, 21, and 28 days of incubation, and dried weights were then measured. The degradation rate was calculated by means of equation (2).

$$Degradation\ ratio\ (\%) = \left(\frac{W_0 - W_D}{W_0}\right) x100 \quad \text{Eq. 2}$$

Where W_0 is the initial weight of the scaffolds and W_D is the weight of the dried scaffolds after incubation for a specific time.

2.10.5. Thermal behavior tests

A DSC-250 from TA instruments equipment was used to find the thermogram profiles of samples in each step of the processing. The samples were analyzed in a range of 10 °C–200 °C, stabilizing the equipment at 10 °C and using a ramp of 10 °C/min. The samples analyzed were the raw material of PCL, PCL dissolved in the solvent mixture, filaments of PCL with and without calcium phosphate, and scaffolds of PCL with and without calcium phosphate. Enthalpy was calculated as the area under the curve of the region in which the phase change was evident.

2.10.6. Mechanical test

Mechanical properties were carried out using Universal test machine (Instron 3366, Instron, MA, USA) under a compression static configuration using a force sensor at a speed of 2 mm/min. Force and displacement were acquired, and Young's modulus and maximum stress at 10% of strain were calculated on minimum five assays.

2.10.7. Fourier transformed infrared spectroscopy (FTIR)

The extracts, CP nanoparticles and scaffolds were analyzed by Fourier transformed infrared spectroscopy (FTIR). The measurements were performed with a spectrometer (Spectrum 2, PerkinElmer) with an attenuated total reflectance accessory. In each sample, at least 3 spectra were obtained at different areas (each spectrum is the average of 100 scans between 400 cm^{-1} to 4000 cm^{-1} with 4 cm^{-1} resolution). Baseline correction and mean spectrum were then calculated using numerical software (Matlab, Mathworks, Mass) [29].

2.11. Statistical analysis

Experimental results were presented as box-whisker plots (median and 25th and 75th percentiles) and compared using 2-tailed Student's test using two-tailed Student's t-test or Mann-Whitney test depending on the evaluated normality of distribution according to KS test. For multiple comparisons, the one-way (ANOVA)/Tukey's honestly significant difference post hoc test was used to detect significant differences between the groups (p 0.05). At least triplicate experiments were performed for each experiment.

3. Results and discussion

3.1. Calcium phosphates nanoparticles, filaments, and scaffolds

The X-ray diffractogram obtained from the powder after combustion and heat treatment at 800 °C for 2 h is shown in Fig. 2. The two main phases of calcium phosphate can be identified as Hidroxyapatite (JCPDS 01-074-0566 HAP) and Calcium Phosphate Tricalcium β (JCPDS 01-070-2065 β-TCP). The calcium phosphate particles showed to have sizes of 42.9 nm ± 1.12 nm, as previously reported [18].

It was possible to obtain PCL filaments containing calcium phosphates (CP) particles inside. Fig. 3 shows a photomicrograph of the filament obtained with its respective EDX elemental maps. The homogeneous distribution of calcium and phosphorus inside the filament can be observed, guaranteeing the same distribution of the calcium phosphates particles. Some particles observed on filament

surfaces correspond to agglomerates whose bigger sizes are in the order of 10 μm. Filament made from particle-free PCL is quite flexible. This behavior is diminished when the filament is obtained with calcium phosphate particles.

Fig. 4 A and B show the scaffolds printed with the filaments without particles (A) and with calcium phosphate particles (B). Both types of scaffolds were printed in a TPMS Gyroid shape and show experimental porosity between 48 and 52% and the characteristic interconnected pores which promotes vascularization and are appropriate for tissue regeneration [30–32]. As the filament without particles is much more flexible, the appearance of the scaffold walls becomes smoother and less geometrically defined, while the scaffold printed with the filament with CP particles shows more roughness on the surface of the walls and a more defined geometrical shape. The average pore size of scaffolds without particles is approximately 1.16 ± 0.05 mm, while in scaffolds with particles the pores have an average size of 1.36 ± 0.01 mm. The pore walls of the scaffolds without particles are approximately 0.72 ± 0.13 mm while the scaffolds with particles have walls of 0.78 ± 0.03 mm thick. The differences between the porosity in both types of scaffolds is doubt to the presence of the particles in the filament. The particles increase the surface roughness of the PCL filament, giving it some stiffness, which manifests itself in some slight differences in the pore size of the particulate scaffolds by preventing elastic recovery of the polymeric material. The pore size variation may occur due to the variable diameter of the produced filament, leading to a different extrusion width and misalignment of the deposited continuous fibers during 3D printing [33]. Usually, scaffolds present pore sizes in the range of 100–10000 μm in order to facilitate vascularization and new tissue formation [7,34]. The pore size design that can achieve both optimal mechanical and biological performance is a complex task and has not been fully addressed [35–37].

3.2. Swelling and degradation properties

Fig. 5A shows the swelling trend of the scaffolds without CP particles and with CP particles after 70 h. There are no significant differences between the groups. Due to an ion exchange between the scaffolds and PBS, a sudden change in swelling occurred for both groups after 5 h. After this time, both groups showed a more or less stable swelling rate due to the stability of ion exchange over time indicating low porosity. The hydrophilic and porous microstructure of the scaffolds leads to absorbing some amount of liquid into the network. Moreover, the ions present in the liquid induce osmotic pressure between the inside and outside of the scaffold network enhanced the water diffusion into the PCL [28]. The pores in the scaffold were filled with PBS in the early stages of the test. It does not appear that such PBS absorption affects the integrity of the scaffold over time. This would suggest that the process of impregnation with the plant extracts would not cause appreciable deterioration of the scaffold over time.

Fig. 5B shows the degradation rate of the PCL and PCL/CP particles scaffolds. It can be observed that the degradation of scaffolds made from pure PCL is very low. The maximum degradation value is 0.26% after 28 days of exposure to the solution. PCL, given its linear and regular structure, is a semi-crystalline polymer and its degradation rate will depend on the degree of crystallinity reached. The more crystalline PCL is, the slower the degradation process. Scaffolds made from PCL with CP particles show a slight increase in degradation. During the first 7 days of exposure to the solution, the maximum degradation measured in the test period is presented, which reaches a value of 1.7%. After that, the degradation value decreases to very low values. The calcium phosphate particles are bioactive [38]. In contact with SBF the calcium phosphates degrade and as a product of this reaction, they form apathetic phases [39, 40] on their surface. The scaffolds containing CP particles have a low percentage of exposed particles on the surface. In the period of time considered in the test, the few particles that are in contact with the physiological fluid undergo the degradation process. Hence the low degradation values and the tendency to present a high initial value.

3.3. Contact angle

Fig. 6 shows the contact angle data boxplot graphics of the samples corresponding to the scaffolds without and with calcium phosphates particles. There is a clear difference between the two populations indicating a decrease in the contact angle with the

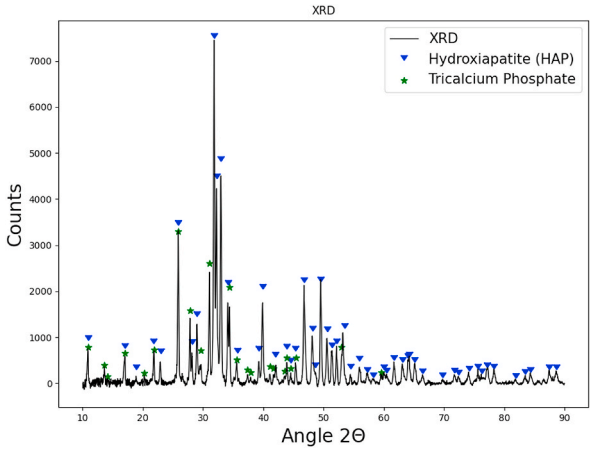

Fig. 2. DRX diffractogram of the calcium phosphate particles synthesized by auto-combustion.

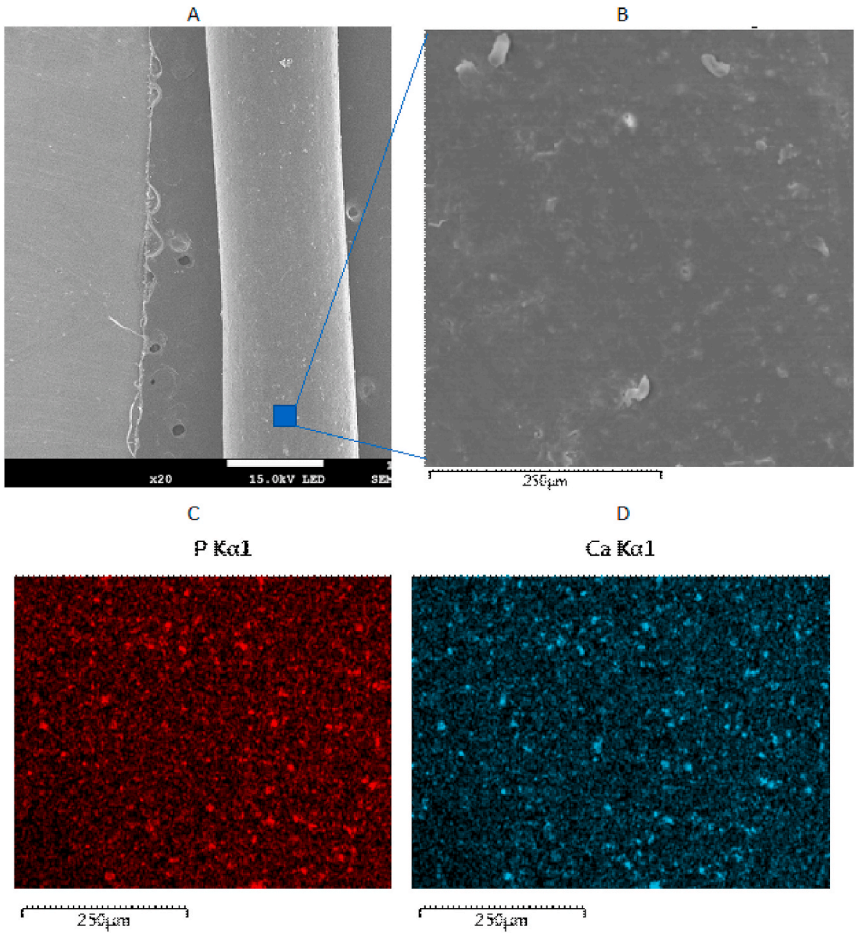

Fig. 3. A) SEM photomicrography of filament obtained with PCL containing calcium phosphates. B) Zoom of the figure where EDX elemental maps were done. C) and D Elemental EDX map for C) Phosphorus D) Calcium.

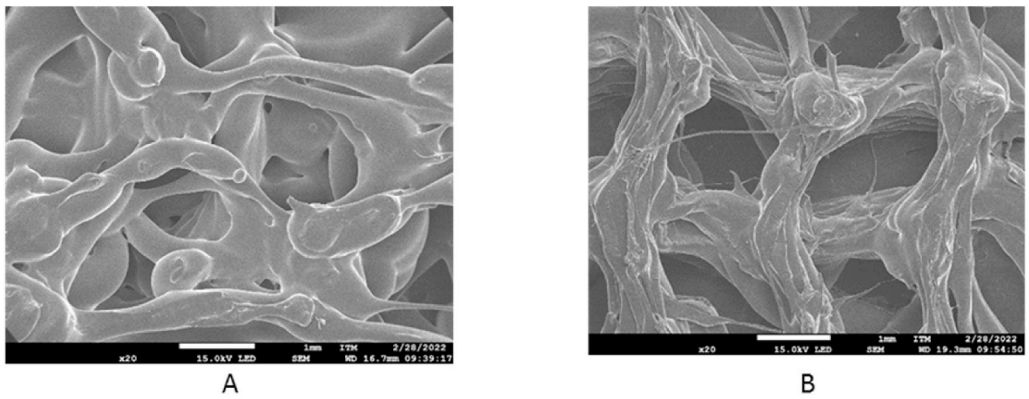

Fig. 4. Scaffolds printed in TPMS gyroid form with the filament of PCL A. without particles of calcium phosphates B. with particles of calcium phosphates.

addition of particles. A p-value of 0.003 was obtained (t-value equal to 4.58 with 7° of freedom) with a confidence value of 95%, thus rejecting the null hypothesis and proving that the two populations are definitely statistically different. The inorganic calcium phosphate particles present in the scaffolds could increase the absorption of the solution through their surface decreasing the contact angle of the scaffolds with the surface and increasing the hydrophilicity of the composite. This could facilitate the scaffolds impregnation process by making a scaffold printed with PCL with calcium phosphates particles to more easily absorb the plant's extracts to be

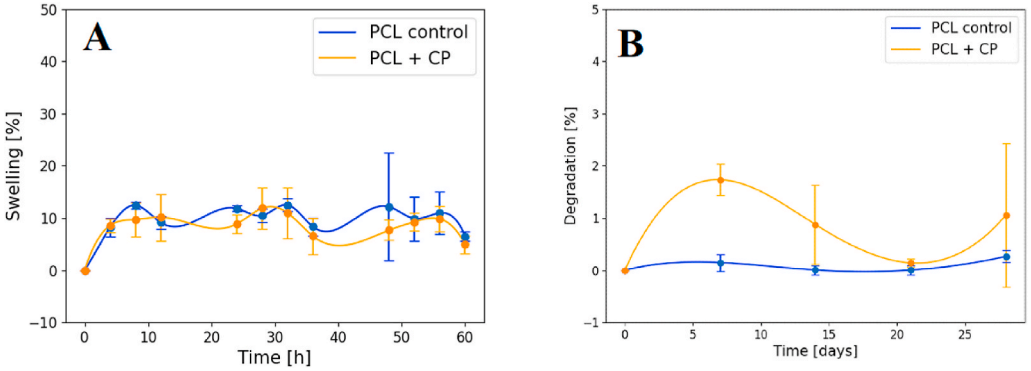

Fig. 5. Graph of the swelling ratio (A) and Degradation properties (B) of scaffolds of PCL without calcium phosphates particles and PCL with calcium phosphates particles.

impregnated.

3.4. Thermal behavior

To evaluate the influence of each of the processes carried out (from the raw material to obtaining the scaffolds), DSC analyses were performed on the materials obtained at each stage of the processing. The DSC profiles of the obtained materials are depicted in Fig. 7.

The crystallinity index (CI) and melting point of every material were determined by DSC. CI was determined using Equation 3

$$CI(\%) = \left(\frac{\Delta H_{exp}}{\Delta H_0 \, x \, f}\right) x100 \qquad \text{Eq. 3}$$

Where H_{exp} is fusion enthalpy (J/g) determined by DSC measurement, H_0 is theoretical enthalpy of the completely crystalline polymer, which is 132 J/g for PCL, and the weight percentage of PCL in each blend is given by the term f [41].

Table 1 shows the melting point, crystallinity index (CI) and fusion enthalpy values of the different materials.

It can be observed that the melting point of polycaprolactone (PCL) does not vary regardless of the thermal processes to which it is subjected during the filament and scaffold fabrication process, or the addition of calcium phosphate nanoparticles. This value is comparable with the values reported in the literature (almost 60 °C) [42].

The crystallinity for pure PCL agreed with the value reported in the literature (approx. 60%) [43,44]. This value is altered by the dissolution process of the material in organic solvents. Such dissolution decreases the crystallinity of the polymer, which is also reflected in a lower crystallinity of the filaments and scaffolds manufactured with this material. However, the presence of the calcium phosphate particles increased the crystallinity of the previously dissolved polymer, reaching values close to those of pure PCL. Probably the presence of the particles increased the interaction between the polymer chains, contributing to a better organization of the polymer and increasing its crystallinity [45–48]. The thermal characteristics of the PCL processed to obtain filaments and then scaffolds, allow us to confirm that the use of relatively low printing temperatures does not cause thermal degradation of the printed materials.

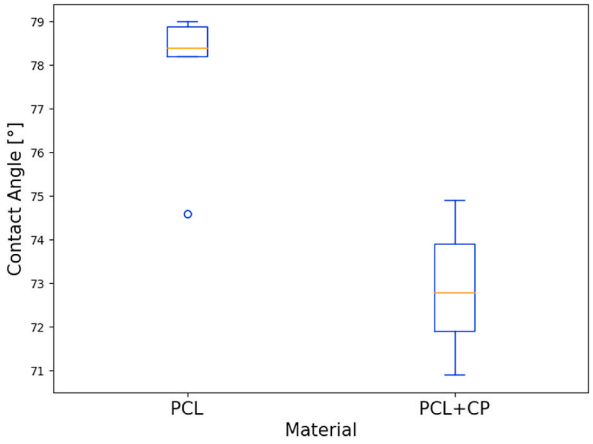

Fig. 6. Contact angle tests data for 3D printed scaffolds with PCL pure and PCL with Calcium phosphates (CP) particles.

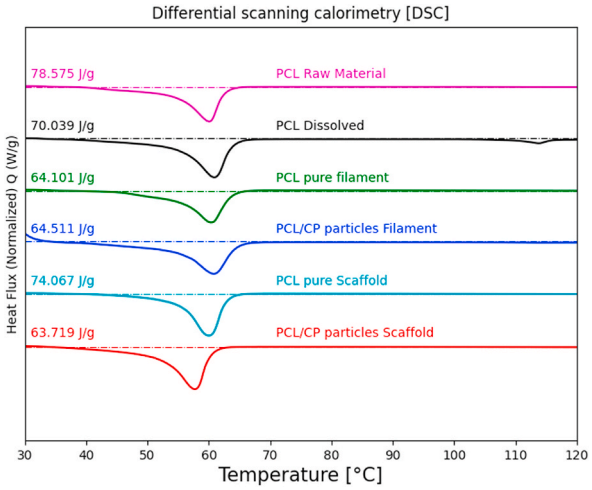

Fig. 7. DSC profiles of the materials obtained in each stage of the processing carried out to obtain PCL scaffolds with and without CP particles.

Table 1
Melting point, Fusion enthalpy Hexp) and Crystallinity index (CI) for the materials obtained in every step of the processing. The CI was calculated from Eq. (1).

Materials	Melting point (°C)	Fusion enthalpy (Hexp) (J/g)	Crystallinity index (CI)
PCL Raw material (pellets)	57.73	78.575	59.526
PCL dissolved in organic solvents	60.00	70.039	53.057
Filament of PCL pure	60.84	64.101	48.561
Filament of PCL/CP particles	60.39	64.511	61.089
Scaffolds with PCL pure	60.89	74.067	56.111
Scaffolds with PCL/CP particles	60.05	63.719	60.339

3.5. *Fourier transformed infrared spectroscopy FTIR*

Fig. 8 shows the FTIR spectra of PCL, CP, J. cf. colorata extract, B. rosea extract and 3D printed scaffold/extracts. The PCL FTIR spectra shows its characteristic infrared bands. It is possible to identify the symmetric (2868 cm-1) and asymmetric (2945 cm-1) CH2 stretching, the carbonyl stretching (1725 cm-1), the CH2 bending (1363 cm-1), the backbone C–O and C–C stretching in the crystalline phase (1292 cm-1), as well as the symmetric and asymmetric C–O–C stretching vibrations (1240 cm-1, 1165 cm-1, 1106 cm-1, 1047 cm-1) [34–37]. The calcium phosphates were identified with high correlation in their fundamental bands 1900 cm-1 ν(OH-), 1161 cm-1 ν(PO43-), 1039 cm-1 ν(PO43-), 900 cm-1 ν(PO43-), and 529 cm-1 ν(OH-) [38]. The pure extracts of J. cf. colorata and B. rosea have very similar FTIR spectra associated with saponin compounds. They have functional groups of 3364 cm-1 hydrophilic sugars (OH-) and a lipophilic part of 2990 cm-1 aromatics, methyls, 1620 cm-1 carbonyls, and 1015 cm-1 ethers. In PCLCP scaffolds

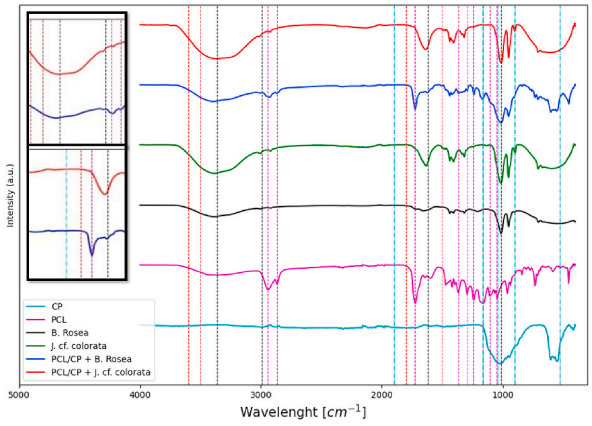

Fig. 8. FTIR spectra profiles of the materials obtained in each stage of the processing carried out to obtain CaP, PCL, Bilia Rose, J. cf. *colorata* and scaffolds with plant extracts.

impregnated with J. cf. colorata, the carbonyl signal (1800–1500 cm-1) disappears by shifting the C]O to the right. In scaffolds impregnated with *B. rosea*, the position and intensity of the PCL carbonyl predominates, masking the carbonyls of the *B. rosea*. The hydroxyl groups (3600-3500 cm^{-1} without hydrogen bonding) of *B. rosea* and *J.* cf. *colorata* maintain the same shape and intensity when impregnated on the scaffolds without significant changes. The OH intensities between 3100 and 3200 cm^{-1} (with hydrogen bonding) are low signals for the plant extracts. In PCLCP scaffolds impregnated with both extracts, these signals are attenuated.

In the 3D printed scaffolds PCLCP + extract, some of the peaks were overlapped and some absorption bands were shifted to higher or lower wavenumber owing to the interaction between the components. Thus, the peak at 1730 cm^{-1} corresponding to ν(C]O) was shifted to a higher wavenumber when the scaffold was impregnated with *B. rosea*. This may be due to the interaction between the plant extract and the composite material. The spectra of the pure extract of *J.* cf. *colorata* and the extract impregnated in the scaffold remain similar, showing low interaction with the composite material of the scaffolds.

3.6. Mechanical properties

The compression force and deformation were recorded. Average stress vs strain curves and their uncertainty (Fig. 9a) for scaffolds PCL and PCL + CP nanoparticles were obtained. Both types of scaffolds exhibited a clear elastoplastic cellular solid behavior (Fig. 9b). Region I corresponds to the initial part of the stress-strain plot, where a positive and high slope is present. In this region, the response is mainly linear elastic. Region II follows the elastic regime and can be characterized by a sudden reduction of the slope, maintaining a linear response corresponding to bending and buckling of the scaffold trusses, leading to plastic deformation. Finally, Region III appears as a further change in slope towards increasing values, corresponding to the final densification of the scaffold. A scaffold is expected to work on Region I to keep the initially intended geometry, allowing cellular and vascular growth inside its porous structure. A linear elastic regime (Region I) describing the pores edge bending of face stretching, a stress plateau (Region II) describing a progressive pore collapse by elastic buckling and permanent deformation, and densification zone (Region III) describing a collapse of the pores, were observed. A short linear elastic regime (Region I), a longer plateau (Region II), and delay of densification (Region III) are obtained by increased pore size. These geometrical effects might improve vascularization and innervation during bone healing.

The compressive strength at 10% strain and Young Modulus from slope of elastic region in the stress-strain curves were calculated (Fig. 9c–d). The median of maximum stress was 4.18 MPa and 4.62 MPa respectively, and the bottom and top edges of the box indicate the 25th and 75th percentiles. In the comparison between the compressive strength of PCL + CP particles and PCL scaffolds, no statistically significant differences were found. The trend of the values of compressive strength and Young's Modulus found in this work, are in agreement with those found by Lu et al. [49]. They found mean values of 3.2 MPa and 4.2 MPa at compressive strength and 44.1 MPa and 72.1 MPa at compressive modulus for PCL pure and 80/20 PCL + HA scaffolds respectively.

The results showed that the incorporation of CP particles in the PLC volume did not affect the compressive strength of scaffolds. However, a light trend to increase the Young modulus might be observed. Although, there were no statistically significant differences. Furthermore, the mechanical response of PCL scaffolds -without any solvent treatment- and PCL/PC scaffolds -with solvent treatment- showed no significant mechanical variations, ruling out the possible detrimental effect of the use of solvents on the mechanical properties of the PCL/PC scaffolds.

3.7. Antibacterial behavior

Concentrated ethanol-soluble extracts of *B. rosea* and *J.* cf. *colorata* were tested using the agar disk diffusion on *S. aureus* and

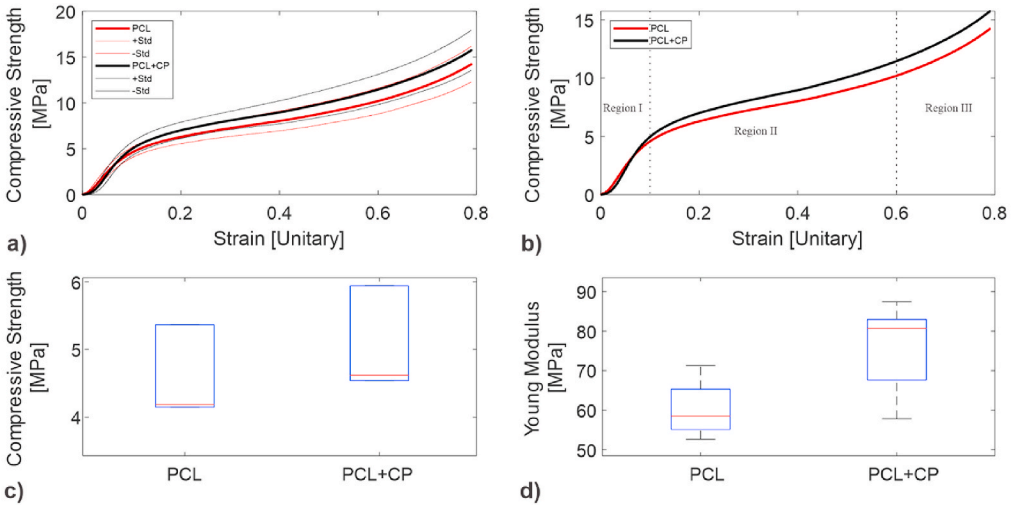

Fig. 9. Mechanical characterization. a) Stress-Strain curves of scaffolds, b) elastoplastic cellular solid behavior, c) compressive strength and d) Young modulus.

S. mutans strains, respectively. *B. rosea* concentrated extract showed a growth inhibition zone on *S. aureus* strain of ~23 mm (Fig. 10a). A similar inhibition zone was not found on the assessed *S. mutans* strain (Fig. 10b). These values were comparable to ZOI values using chlorhexidine, a widely used positive control. No inhibition zone was observed in the negative control. A serial dilution between 50% w/v to 1% w/v was conducted for *B. rosea*. In those cases, ZOI decreased exhibiting a non-linear tendency (data not shown). The minimum inhibitory concentration (MIC) of *B. rosea* was 6 mg/mL. The percentage relative to inhibition growth of *S. aureus* of PLC + CP discs impregnated with 4X and 2X (80 μl) of *B. rosea* were 53% and 32%, respectively (Fig. 10c and d). These results are promising, since there are no previous reports of a selective inhibitory activity of *B. rosea* against *S aureus.*

Otherwise, *J.* cf. *colorata* concentrated extract did not show inhibitory effects on *S. aureus* nor *S. mutans*. Although this species is known as "antibiotic" by local communities in Colombia, the results did not validate its traditional use. However, more studies could be conducted to validate its antimicrobial potential against other bacterial strains, since ethnopharmacological information of related species, evidenced antibacterial properties in leaves and stems of *J. pectoralis* [50]. This bioactivity was also reported by other authors, in which a high inhibitory activity of the ethyl acetate-soluble leaf extract of *J. pectoralis* against *Escherichia coli*, *E. faecalis*, and *Staphylococcus epidermidis*, was obtained [51]. Overall, it is therefore relevant to consider that the chemical composition of plant extracts may vary within species of the same genus, and that the antibacterial activity can be selective against different strains.

3.8. Chemical characterization of B. rosea and J. cf. colorata

For both crude extracts, a partial detection of compounds was achieved by GCMS. With this analytical technique, volatile and thermally stable metabolites can be separated and detected, but not other compounds.

For *J.* cf. *colorata*, most of the compounds detected using GCMS were fatty acids [42]. A relevant finding was the presence of a minor compound (40,887 min; relative intensity 0,70%) with fragment ions at *m/z* 157 and 115, suggesting a quinoline moiety with two methyl groups. Quinoline alkaloids, are N-based heterocyclic compounds derived from the amino acid tryptophan [50]. Over 200 structures of these alkaloids have been isolated, with a wide range of activities, including antibacterial effects [51]. In this way, quinoline alkaloids have been identified in other Justicia species [52], which suggests that the presence of a quinoline alkaloid, as detected by GCMS, could be affecting the bacterial growth in this study. This finding is in accordance with the literature, where quinoline alkaloids have been identified in other *Justicia* species [53]. In fact, related quinolone alkaloids target bacterial type IIA topoisomerase/gyrase [54]. Furthermore, antibiotics such as metronidazole, are derived from the synthesis of quinine, a quinoline alkaloid [53]. In this study, the low relative intensity of the quinoline moiety detected, indicates a low concentration in the crude extract, and as a result its poor effect in the bioassays. Other extraction methods or bioassay-guided isolation are recommended to validate the traditional use of this plant, as antibiotic.

For *B rosea*, the monoterpene limonene (relative intensity 0,96%), the diterpene phytol (2,55%), phenolic acids, fatty acid esters, squalene (8,57%), and other prenylated lipids, were detected with GCMS (Fig. 11). Not much has been reported in the phytochemistry of *B. rosea*, except for triterpene saponins isolated from its seeds. In particular, billiosides B and C, inhibited glucose intestinal absorption in rats and the enzyme glucose-6-phosphatase [55]. However, triterpene saponins isolated from other species of Sapindaceae or other families, were reported for its inhibitory activity against gram-positive and gram-negative bacteria [56]. The prenylated lipids detected in this study after 40 min in the chromatogram presented in Fig. 11, including phytol and squalene, could support the presence of biosynthetic related compounds. Although inconclusively, in de mass spectral information, fragment ions at *m/z* 231, 189 and 73, suggest triterpene moieties, as part of the aglycone structure that could be detected with the conditions used for the GCMS. The promising bioactivity results obtained and the detection of its precursor, squalene, and other prenylated lipids, could suggest the presence of triterpene saponins in the studied sample of *B. rosea*. More studies are needed to characterize the compounds involved in its antibacterial activity.

4. Conclusions

Nanoparticles of calcium phosphates were synthesized by the auto-combustion method. Calcium phosphate nanoparticles were used to form a polycaprolactone filament loaded with 20% w/w of particles. With this filament, scaffolds were printed in the form of TPMS Gyroid, with walls of 0.72–0.78 mm thick and pores of 1.16–1.36 mm in diameter. Two Colombian plants *Justicia* cf *colorifera* (Acanthaceae), and *Billia rosea* (Sapindaceae) were chosen to obtain extracts and evaluate their bactericidal action. The extracts were loaded onto the scaffolds using a vacuum impregnation method that was facilitated because the hydrophilicity of the PCL was slightly increased by the presence of the inorganic material inside the PCL filament. The method used to load the extracts onto the scaffolds did not accelerate the degradation of the scaffolds significantly. Likewise, the presence of the calcium phosphate particles in the scaffolds did not affect their compressive strength notably. Both the ethanol-soluble extract, as well as the scaffolds loaded with *B. rosea* extract exhibited significant bactericidal action when tested against *S. aureus* and *S. mutans* strains. In the chemical composition, some prenylated compounds were detected, suggesting the presence of terpenoid saponins, compounds with antibacterial potential, reported for *B. rosea.* Otherwise, *J.* cf. *colorata* concentrated extract did not show inhibitory effects against *S. aureus* nor *S. mutans*. Although this species is known as "antibiotic" by local communities in Colombia, the results did not validate its traditional use. However, in the GCMS analysis a quinoline moiety was detected, which could lead to further studies since quinoline alkaloids have reports as antibiotics. In addition, more studies could be conducted to validate its antimicrobial potential of this species against other bacterial strains.

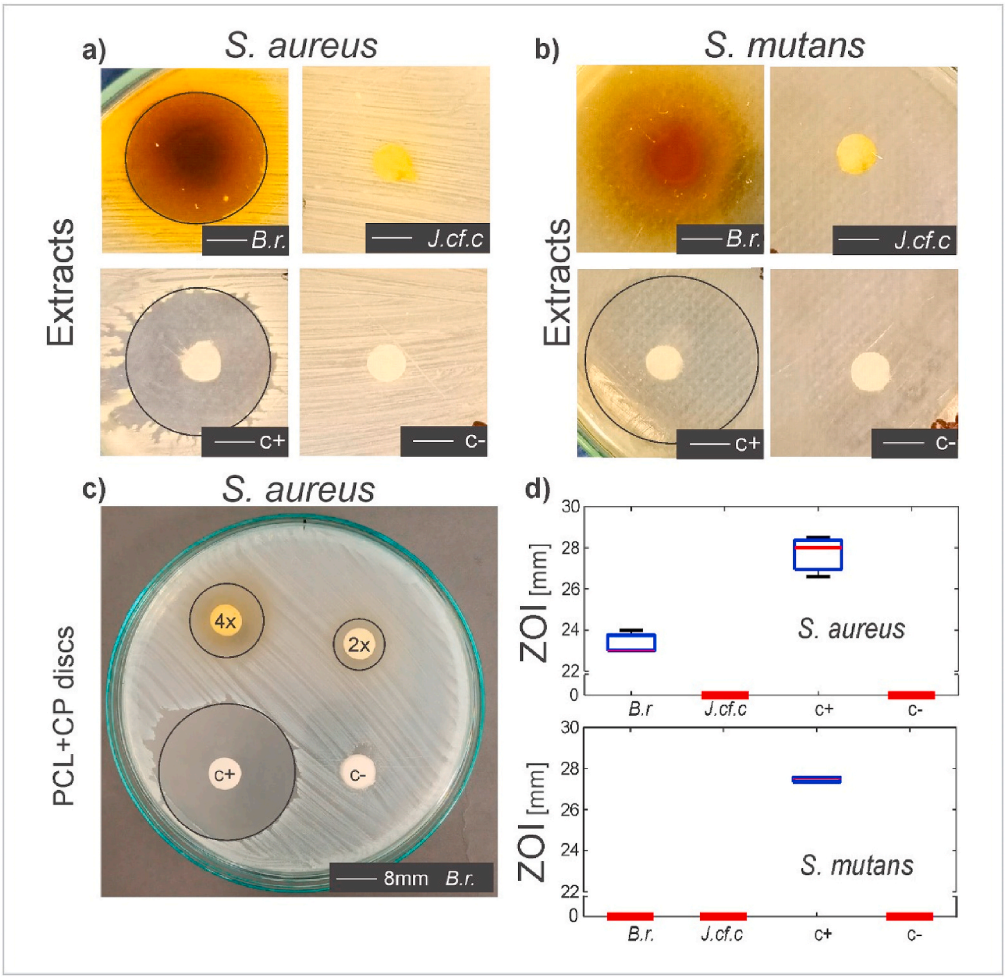

Fig. 10. Rapid screening of ZOI on a) *S. aureus and b) S. mutans strain, of* experimental concentrated extracts: *B. rosea (B.r.) and J.* cf. *colorata (J.* cf *c.), positive control (c+: chlorhexidine) and negative control (c-: DMSO). c) PCL + CP impregnated discs with B. rosea extract. d) Statistical analysis of the results.*

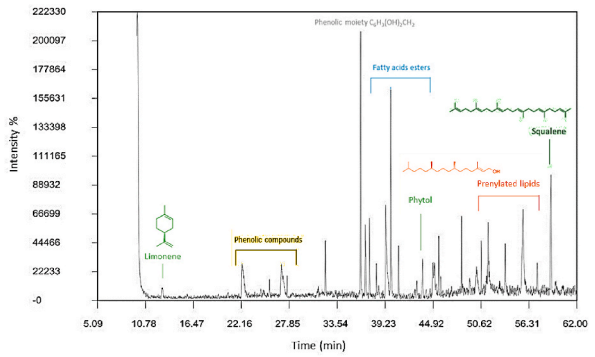

Fig. 11. Chromatogram obtained with GCMS of *Billia rosea* extract.

Author contribution statement

Yeison Orozco, Alejandra Betancur, Ana Isabel Moreno, Katherine Fuentes: Performed the experiments.
Alex Lopera: Analyzed and interpreted the data; Contributed reagents, materials, analysis tools or data.

Oscar Suarez: Contributed reagents, materials, analysis tools or data.

Tatiana Lobo, Alexander Ossa, Alejandro Peláez-Vargas, Carlos Paucar, Claudia Garcia: Conceived and designed the experiments; Analyzed and interpreted the data; Contributed reagents, materials, analysis tools or data; Wrote the paper.

Funding statement

Carlos Paucar was supported by Universidad Nacional de Colombia [Hermes 47177]. Alejandro Pelaez-Vargas was supported by Universidad Cooperativa de Colombia [2830]. Professor Claudia Garcia was supported by Ministerio de Ciencia, Tecnología e Innovación (MINCIENCIAS) [Project 71203, 80740-476-2020].

Data availability statement

No data was used for the research described in the article.

Declaration of interest's statement

The authors declare no competing interests.

References

[1] J. Russias, E. Saiz, S. Deville, K. Gryn, G. Liu, R.K. Nalla, A.P. Tomsia, Fabrication and in vitro characterization of three-dimensional organic/inorganic scaffolds by robocasting, J. Biomed. Mater. Res. 83A (2007) 434–445, https://doi.org/10.1002/jbm.a.31237.

[2] D.S. Larionov, M.A. Kuzina, P.V. Evdokimov, A.V. Garshev, N.K. Orlov, V.I. Putlyaev, Synthesis of calcium phosphate powders in nonaqueous media for stereolithography 3D printing, Russ. J. Inorg. Chem. 65 (2020) 312–322, https://doi.org/10.1134/S0036023620030079.

[3] M.-J. Chern, L.-Y. Yang, Y.-K. Shen, J.-H. Hung, 3D scaffold with PCL combined biomedical ceramic materials for bone tissue regeneration, Int. J. Precis. Eng. Manuf. 14 (2013) 2201–2207, https://doi.org/10.1007/s12541-013-0298-1.

[4] S. Liu, S. Qin, M. He, D. Zhou, Q. Qin, H. Wang, Current applications of poly(lactic acid) composites in tissue engineering and drug delivery, Compos. B Eng. 199 (2020), 108238, https://doi.org/10.1016/j.compositesb.2020.108238.

[5] P. Sheshadri, R.A. Shirwaiker, Characterization of material–process–structure interactions in the 3D bioplotting of polycaprolactone, 3D Print. Addit. Manuf. 2 (2015) 20–31, https://doi.org/10.1089/3dp.2014.0025.

[6] R. Roque, G.F. Barbosa, A.C. Guastaldi, Design and 3D bioprinting of interconnected porous scaffolds for bone regeneration. An additive manufacturing approach, J. Manuf. Process. 64 (2021) 655–663, https://doi.org/10.1016/j.jmapro.2021.01.057.

[7] Y. Zhang, N. Sun, M. Zhu, Q. Qiu, P. Zhao, C. Zheng, Q. Bai, Q. Zeng, T. Lu, The contribution of pore size and porosity of 3D printed porous titanium scaffolds to osteogenesis, Biomater. Adv. 133 (2022), 112651, https://doi.org/10.1016/j.msec.2022.112651.

[8] J.A. Ramírez, V. Ospina, A.A. Rozo, M.I. Viana, S. Ocampo, S. Restrepo, N.A. Vásquez, C. Paucar, C. García, Influence of geometry on cell proliferation of PLA and alumina scaffolds constructed by additive manufacturing, J. Mater. Res. 34 (2019) 3757–3765, https://doi.org/10.1557/jmr.2019.323.

[9] R.A. García-León, J.A. Gómez-Camperos, H.Y. Jaramillo, Scientometric review of trends on the mechanical properties of additive manufacturing and 3D printing, J. Mater. Eng. Perform. 30 (2021) 4724–4734, https://doi.org/10.1007/s11665-021-05524-7.

[10] A. Sadeghianmaryan, S. Naghieh, Z. Yazdanpanah, H. Alizadeh Sardroud, N.K. Sharma, L.D. Wilson, X. Chen, Fabrication of chitosan/alginate/hydroxyapatite hybrid scaffolds using 3D printing and impregnating techniques for potential cartilage regeneration, Int. J. Biol. Macromol. 204 (2022) 62–75, https://doi.org/10.1016/j.ijbiomac.2022.01.201.

[11] P. Feng, K. Wang, Y. Shuai, S. Peng, Y. Hu, C. Shuai, Hydroxyapatite nanoparticles in situ grown on carbon nanotube as a reinforcement for poly (ε-caprolactone) bone scaffold, Mater. Today Adv. 15 (2022), 100272, https://doi.org/10.1016/j.mtadv.2022.100272.

[12] C. Shuai, W. Yang, P. Feng, S. Peng, H. Pan, Accelerated degradation of HAP/PLLA bone scaffold by PGA blending facilitates bioactivity and osteoconductivity, Bioact. Mater. 6 (2021) 490–502, https://doi.org/10.1016/j.bioactmat.2020.09.001.

[13] P. Feng, P. Wu, C. Gao, Y. Yang, W. Guo, W. Yang, C. Shuai, A multimaterial scaffold with tunable properties: toward bone tissue repair, Adv. Sci. 5 (2018), 1700817, https://doi.org/10.1002/advs.201700817.

[14] C. Shuai, B. Peng, P. Feng, L. Yu, R. Lai, A. Min, In situ synthesis of hydroxyapatite nanorods on graphene oxide nanosheets and their reinforcement in biopolymer scaffold, J. Adv. Res. 35 (2022) 13–24, https://doi.org/10.1016/j.jare.2021.03.009.

[15] X. Wang, B.Z. Molino, S. Pitkänen, M. Ojansivu, C. Xu, M. Hannula, J. Hyttinen, S. Miettinen, L. Hupa, G. Wallace, 3D scaffolds of polycaprolactone/copper-doped bioactive glass: architecture engineering with additive manufacturing and cellular assessments in a coculture of bone marrow stem cells and endothelial cells, ACS Biomater. Sci. Eng. 5 (2019) 4496–4510, https://doi.org/10.1021/acsbiomaterials.9b00105.

[16] P. Nevado, A. Lopera, V. Bezzon, M.R. Fulla, J. Palacio, M.A. Zaghete, G. Biasotto, A. Montoya, J. Rivera, S.M. Robledo, H. Estupiñan, C. Paucar, C. Garcia, Preparation and in vitro evaluation of PLA/biphasic calcium phosphate filaments used for fused deposition modelling of scaffolds, Mater. Sci. Eng. C 114 (2020), 111013, https://doi.org/10.1016/j.msec.2020.111013.

[17] F.D. Cojocaru, V. Balan, M.I. Popa, A. Lobiuc, A. Antoniac, I.V. Antoniac, L. Verestiuc, Biopolymers – calcium phosphates composites with inclusions of magnetic nanoparticles for bone tissue engineering, Int. J. Biol. Macromol. 125 (2019) 612–620, https://doi.org/10.1016/j.ijbiomac.2018.12.083.

[18] A.A. Lopera, A. Montoya, I.D. Vélez, S.M. Robledo, C.P. Garcia, Synthesis of calcium phosphate nanostructures by combustion in solution as a potential encapsulant system of drugs with photodynamic properties for the treatment of cutaneous leishmaniasis, Photodiagnosis Photodyn. Ther. 21 (2018) 138–146, https://doi.org/10.1016/j.pdpdt.2017.11.017.

[19] M.B. Hajduga, R. Bobiński, M. Dutka, I. Ulman-Włodarz, J. Bujok, C. Pająk, M. Ćwiertnia, A. Kurowska, M. Dziadek, I. Rajzer, Analysis of the antibacterial properties of polycaprolactone modified with graphene, bioglass and zinc-doped bioglass, Acta Bioeng. Biomech. 23 (2021), https://doi.org/10.37190/ABB-01766-2020-03.

[20] Y. Zhuang, K. Lin, H. Yu, Advance of nano-composite electrospun fibers in periodontal regeneration, Front. Chem. (2019) 7. https://www.frontiersin.org/articles/10.3389/fchem.2019.00495.

[21] M. Reise, R. Wyrwa, U. Müller, M. Zylinski, A. Völpel, M. Schnabelrauch, A. Berg, K.D. Jandt, D.C. Watts, B.W. Sigusch, Release of metronidazole from electrospun poly(l-lactide-co-d/l-lactide) fibers for local periodontitis treatment, Dent. Mater. 28 (2012) 179–188, https://doi.org/10.1016/j.dental.2011.12.006.

[22] M.A. Fanovich, J. Ivanovic, D. Misic, M.V. Alvarez, P. Jaeger, I. Zizovic, R. Eggers, Development of polycaprolactone scaffold with antibacterial activity by an integrated supercritical extraction and impregnation process, J. Supercrit. Fluids 78 (2013) 42–53, https://doi.org/10.1016/j.supflu.2013.03.017.

[23] S. Naderi, A. Esmaeili, Fabrication and characterization of 3D printing scaffold technology by extract oils from plant and its applications in the cardiovascular blood, Sci. Rep. 11 (2021), 24409, https://doi.org/10.1038/s41598-021-03951-z.

[24] B.R.N. Soumya, S. L, Antifungal efficacy of Capsicum frutescens L. extracts against some prevalent fungal strains associated with groundnut storage, J. Agric. Techn. 8 (2012) 739–750.

[25] G. Sharmila, C. Muthukumaran, S. Kirthika, S. Keerthana, N.M. Kumar, J. Jeyanthi, Fabrication and characterization of Spinacia oleracea extract incorporated alginate/carboxymethyl cellulose microporous scaffold for bone tissue engineering, Int. J. Biol. Macromol. 156 (2020) 430–437, https://doi.org/10.1016/j.ijbiomac.2020.04.059.

[26] E.A. Chavarriaga, A.A. Lopera, T. Bender Wermuth, S. Arcaro, V.D.N. Bezzon, C. García, J. Alarcón, J. Gabriel Ramirez, R. Moreno, C. Pérez Bergmann, Influence of caffeine and citrulline on magnetic properties when used as new fuels in the synthesis of CoFe2O4 nanoparticles by gel combustion, J. Magn. Magn Mater. 560 (2022), 169632, https://doi.org/10.1016/j.jmmm.2022.169632.

[27] A.E. Jakus, A.L. Rutz, R.N. Shah, Advancing the field of 3D biomaterial printing, Biomed. Mater. 11 (2016), 014102, https://doi.org/10.1088/1748-6041/11/1/014102.

[28] P. Rahmani, A. Shojaei, Developing tough terpolymer hydrogel with outstanding swelling ability by hydrophobic association cross-linking, Polymer 254 (2022), 125037, https://doi.org/10.1016/j.polymer.2022.125037.

[29] A. Pelaez-Vargas, J.A. Dussan, L.F. Restrepo-Tamayo, C. Paucar, J.A. Ferreira, F.J. Monteiro, The effect of slurry preparation methods on biaxial flexural strength of dental porcelain, J. Prosthet. Dent 105 (2011) 308–314, https://doi.org/10.1016/S0022-3913(11)60058-9.

[30] J. Santos, T. Pires, B.P. Gouveia, A.P.G. Castro, P.R. Fernandes, On the permeability of TPMS scaffolds, J. Mech. Behav. Biomed. Mater. 110 (2020), 103932, https://doi.org/10.1016/j.jmbbm.2020.103932.

[31] T. Pires, J. Santos, R.B. Ruben, B.P. Gouveia, A.P.G. Castro, P.R. Fernandes, Numerical-experimental analysis of the permeability-porosity relationship in triply periodic minimal surfaces scaffolds, J. Biomech. 117 (2021), 110263, https://doi.org/10.1016/j.jbiomech.2021.110263.

[32] Y. Lv, B. Wang, G. Liu, Y. Tang, J. Liu, G. Wei, L. Wang, Design of bone-like continuous gradient porous scaffold based on triply periodic minimal surfaces, J. Mater. Res. Technol. 21 (2022) 3650–3665, https://doi.org/10.1016/j.jmrt.2022.10.160.

[33] S.K. Hedayati, A.H. Behravesh, S. Hasannia, O. Kordi, M. Pourghaumi, A.B. Saed, F. Gashtasbi, Additive manufacture of PCL/nHA scaffolds reinforced with biodegradable continuous Fibers: mechanical Properties, in-vitro degradation Profile, and cell study, Eur. Polym. J. 162 (2022), 110876, https://doi.org/10.1016/j.eurpolymj.2021.110876.

[34] T. Kokubo, H.-M. Kim, M. Kawashita, Novel bioactive materials with different mechanical properties, Biomaterials 24 (2003) 2161–2175, https://doi.org/10.1016/S0142-9612(03)00044-9.

[35] V. Karageorgiou, D. Kaplan, Porosity of 3D biomaterial scaffolds and osteogenesis, Biomaterials 26 (2005) 5474–5491, https://doi.org/10.1016/j.biomaterials.2005.02.002.

[36] Â. Semitela, A.F. Girão, C. Fernandes, G. Ramalho, I. Bdikin, A. Completo, P.A. Marques, Electrospinning of bioactive polycaprolactone-gelatin nanofibres with increased pore size for cartilage tissue engineering applications, J. Biomater. Appl. 35 (2020) 471–484, https://doi.org/10.1177/0885328220940194.

[37] R. Liu, L. Ma, H. Liu, B. Xu, C. Feng, R. He, Effects of pore size on the mechanical and biological properties of stereolithographic 3D printed HAp bioceramic scaffold, Ceram. Int. 47 (2021) 28924–28931, https://doi.org/10.1016/j.ceramint.2021.07.053.

[38] S. Cai, G.H. Xu, X.Z. Yu, W.J. Zhang, Z.Y. Xiao, K.D. Yao, Fabrication and biological characteristics of β-tricalcium phosphate porous ceramic scaffolds reinforced with calcium phosphate glass, J. Mater. Sci. Mater. Med. 20 (2009) 351–358, https://doi.org/10.1007/s10856-008-3591-2.

[39] J. Suwanprateeb, R. Sanngam, W. Suvannapruk, T. Panyathanmaporn, Mechanical and in vitro performance of apatite–wollastonite glass ceramic reinforced hydroxyapatite composite fabricated by 3D-printing, J. Mater. Sci. Mater. Med. 20 (2009) 1281–1289, https://doi.org/10.1007/s10856-009-3697-1.

[40] E.H. Backes, E.M. Fernandes, G.S. Diogo, C.F. Marques, T.H. Silva, L.C. Costa, F.R. Passador, R.L. Reis, L.A. Pessan, Engineering 3D printed bioactive composite scaffolds based on the combination of aliphatic polyester and calcium phosphates for bone tissue regeneration, Mater. Sci. Eng. C 122 (2021), 111928, https://doi.org/10.1016/j.msec.2021.111928.

[41] A.C. Correa, V.B. Carmona, J.A. Simão, L.H. Capparelli Mattoso, J.M. Marconcini, Biodegradable blends of urea plasticized thermoplastic starch (UTPS) and poly (ε-caprolactone) (PCL): morphological, rheological, thermal and mechanical properties, Carbohydr. Polym. 167 (2017) 177–184, https://doi.org/10.1016/j.carbpol.2017.03.051.

[42] S. Jana, M. Leung, J. Chang, M. Zhang, Effect of nano- and micro-scale topological features on alignment of muscle cells and commitment of myogenic differentiation, Biofabrication 6 (2014), 035012, https://doi.org/10.1088/1758-5082/6/3/035012.

[43] C.B.B. Luna, D.D. Siqueira, E. da S.B. Ferreira, E.M. Araújo, R.M.R. Wellen, Effect of injection parameters on the thermal, mechanical and thermomechanical properties of polycaprolactone (PCL), J. Elastomers Plastics 53 (2021) 1045–1062, https://doi.org/10.1177/00952443211015345.

[44] D. Rosa, C. Guedes, M. Bardi, Evaluation of thermal, mechanical and morphological properties of PCL/CA and PCL/CA/PE-g-GMA blends, Polym. Test. 26 (2007) 209–215.

[45] K. Čech Barabaszová, S. Holešová, M. Hundáková, V. Mohyla, Mechanically treated vermiculite particles in PCL/vermiculite thin films, Mater. Today Proc. 52 (2022) 239–247, https://doi.org/10.1016/j.matpr.2022.02.195.

[46] X. Wang, M. Jiang, Z. Zhou, J. Gou, D. Hui, 3D printing of polymer matrix composites: a review and prospective, Compos. B Eng. 110 (2017) 442–458, https://doi.org/10.1016/j.compositesb.2016.11.034.

[47] J. Jordan, K.I. Jacob, R. Tannenbaum, M.A. Sharaf, I. Jasiuk, Experimental trends in polymer nanocomposites—a review, Mater. Sci. Eng. 393 (2005) 1–11, https://doi.org/10.1016/j.msea.2004.09.044.

[48] K. Taleb, I. Pillin, Y. Grohens, S. Saidi-Besbes, Polylactic acid/Gemini surfactant modified clay bio-nanocomposites: morphological, thermal, mechanical and barrier properties, Int. J. Biol. Macromol. 177 (2021) 505–516, https://doi.org/10.1016/j.ijbiomac.2021.02.135.

[49] L. Lu, Q. Zhang, D.M. Wootton, R. Chiou, D. Li, B. Lu, P.I. Lelkes, J. Zhou, Mechanical study of polycaprolactone-hydroxyapatite porous scaffolds created by porogen-based solid freeform fabrication method, J. Appl. Biomater. Funct. Mater. 12 (2014) 145–154, https://doi.org/10.5301/jabfm.5000163.

[50] P.M. Dewick, Medicinal Natural Products, John Wiley & Sons, Ltd, Chichester, UK, 2009, https://doi.org/10.1002/9780470742761.

[51] X.-F. Shang, S.L. Morris-Natschke, Y.-Q. Liu, X. Guo, X.-S. Xu, M. Goto, J.-C. Li, G.-Z. Yang, K.-H. Lee, Biologically active quinoline and quinazoline alkaloids part I, Med. Res. Rev. 38 (2018) 775–828, https://doi.org/10.1002/med.21466.

[52] G.M. Corrêa, A.F. Alcântara, Chemical constituents and biological activities of species of Justicia: a review, Revista Brasileira de Farmacognosia 22 (2012) 220–238.

[53] L.A. Mitscher, Bacterial topoisomerase inhibitors: quinolone and pyridone antibacterial agents, Chem. Rev. 105 (2005) 559–592, https://doi.org/10.1021/cr030101q.

[54] T.P.T. Cushnie, B. Cushnie, A.J. Lamb, Alkaloids: an overview of their antibacterial, antibiotic-enhancing and antivirulence activities, Int. J. Antimicrob. Agents 44 (2014) 377–386, https://doi.org/10.1016/j.ijantimicag.2014.06.001.

[55] A.E.M. Biang, E.L.D. Kamto, L.M. Simo, C. Antheaume, P. Lavedan, M. Vedrenne, O.P. Noté, D.E. Pegnyemb, J.N. Mbing, M. Haddad, Triterpenoid saponins from the stem barks of Chytranthus klaineanus, Radlk. ex Engl, Phytochemistry Letters 37 (2020) 37–41, https://doi.org/10.1016/j.phytol.2020.04.006.

[56] N. Asati, R.N. Yadava, Antibacterial activity of a triterpenoid saponin from the stems of Caesalpinia pulcherrima Linn, Nat. Prod. Res. 32 (2018) 499–507.